

Full-Spectrum Machine Learning Diagnostics for Interstellar PAHs

Zhao Wang^{1,*}

¹ Laboratory for Relativistic Astrophysics, Department of Physics, Guangxi University, Nanning 530004, China

Traditional interstellar polycyclic aromatic hydrocarbon (PAH) diagnostics rely on empirical band ratios, which often suffer from information loss and sample-selection bias. We introduce a machine learning framework that bypasses these limitations by treating the complete 2.75–20 μm emission spectrum as a high-dimensional fingerprint. Using a Random Forest classifier trained on a dataset of 23 653 spectra, we achieve a robust classification F1-score of ~ 0.96 across 12 size and charge categories. Our model maintains high performance on synthetic mixtures of “unseen” molecules. Feature importance analysis reveals that PAH size diagnostics are not universal but highly charge-dependent; while neutral size is traced mainly by C–H stretching modes, sizing ionized species also relies on the morphology of 6–8 μm C–C complexes, with the 12.5 μm feature emerging as a robust cross-charge tracer. This approach provides a robust, data-driven pathway for decoding the physical conditions of the interstellar medium.

INTRODUCTION

Interstellar polycyclic aromatic hydrocarbons (PAHs) are primary subjects of astrophysical study via their infrared (IR) emission (Leger and Puget 1984, Allamandola *et al.* 1985). Their characteristic mid-IR features, notably at 3.3, 6.2, 7.7, 8.6, 11.2, and 12.7 μm are ubiquitous, appearing in diverse environments ranging from individual stellar sources to entire galaxies (Peeters *et al.* 2002, Smith *et al.* 2007). Since PAH size and ionization state are sensitive to the local ultraviolet (UV) field and electron density (Bakes and Tielens 1994, Allamandola *et al.* 1999), these molecules serve as vital diagnostics for energetic regions such as photodissociation regions (PDRs) and active galactic nuclei (Tielens 2008, Li 2020).

Historically, inferring PAH properties from observations relied on empirical band ratios calibrated against limited laboratory or theoretical datasets (Draine and Li 2001). These ratios are grounded in physical principles: for instance, the $I_{11.2}/I_{3.3}$ ratio typically increases with PAH size. This occurs because smaller PAHs reach higher peak temperatures upon stochastic heating by a single photon, which preferentially excites the 3.3 μm C–H stretch over the 11.2 μm out-of-plane bending mode (Allamandola *et al.* 1989, Schutte *et al.* 1993). However, condensing a complex spectrum into a single ratio discards valuable information in band profiles and weaker features, leading to degeneracies and a heightened sensitivity to noise (Boersma *et al.* 2018, Maragkoudakis *et al.* 2020, Bauschlicher Jr. *et al.* 2008, Ricca *et al.* 2012). While the NASA Ames PAH IR Spectroscopic Database (PAHdb) has facilitated more systematic population-based calibrations (Bauschlicher Jr. and Ricca 2010, Boersma *et al.* 2014), band-ratio analysis remains the current, despite limited, standard (Peeters *et al.* 2017).

Figure 1 demonstrates a critical shortcoming of the ratio-based paradigm: its perceived accuracy is often a byproduct of sample selection. For example, Maragkoudakis *et al.* (2020) derived a parametric model for the

$I_{11.2}/I_{3.3}$ –size trend that performed well ($R^2 = 0.822$) when applied to a specific subset of 81 neutral solo-CH PAHs. However, when this same relation is applied to a more comprehensive and randomly sampled dataset of 15 022 neutral PAHs, the correlation weakens significantly and the scatter increases dramatically ($R^2 = 0.230$). This pronounced sensitivity to sample representativeness, coupled with the information loss inherent in reducing complex spectral profiles to discrete band ratios, underscores the necessity of transitioning toward full-spectrum inference methods.

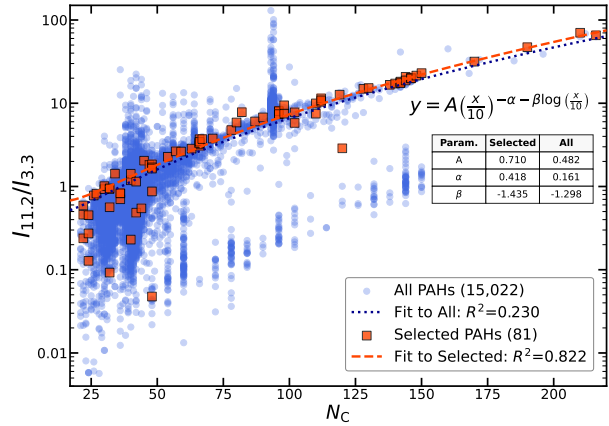


FIG. 1. The emission intensity ratio $I_{11.2}/I_{3.3}$ plotted against the number of carbon atoms (N_C). Circles represent the full dataset of 15 022 neutral PAHs, while squares indicate the 81 PAHs selected by Maragkoudakis *et al.* (2020). All spectra were re-computed using a 6 eV cascade model. The lines depict the fit (parameters in the inset), where the R^2 values highlight the fitting quality.

The advent of machine learning (ML) in astrophysics, together with the expansive PAH spectral library and JWST observatorions, provides a timely opportunity to move beyond traditional band-ratio diagnostics. Here we shift PAH property inference to *full-spectrum* morphology, treating the complete 2.75–20 μm emission spectrum as a high-dimensional fingerprint that can be mapped to

PAH size and charge. Specifically, we train an ML classifier on a large set of single-PAH spectra and evaluate it on observation-like mixtures constructed from unseen PAHs, aiming to provide more accurate, robust, and probabilistic constraints on PAH properties. Importantly, our approach remains physically interpretable: using feature-importance analysis, we identify the wavelength regions that drive the predictions, providing insights into which vibrational bands carry the most diagnostic information.

METHODOLOGY

We developed a data-driven pipeline to infer PAH size and charge from IR emission spectra, integrating a large spectral library with a Random Forest (RF) classifier. The model was trained on individual molecular spectra and validated on synthetic mixtures drawn from an independent “unseen” molecular pool.

The dataset comprises 23 653 unique PAH structures compiled from two sources:

- **PAHdb Theoretical Spectra (v4.0):** 10 404 spectra covering charge states from -1 to $+2$ (Ricca *et al.* 2026).
- **DFT-Calculated Spectra:** 13 986 spectra (B3LYP/4-31G and B3LYP/6-311+G*), with frequencies empirically scaled by 0.9578 and 0.9757, respectively (Bauschlicher and Langhoff 1997).

Ground-state absorption spectra were converted to astrophysical emission using the thermal-cascade approximation via the AmesPAHdbIDLSuite (Boersma *et al.* 2014) at an excitation energy of 6 eV. Additional models at 3 and 9 eV were generated for sensitivity testing (see Supplementary Information, available after peer review).

We focused on the 2.75–20 μm window. Spectra were binned to a grid (20 cm^{-1} width after a sensitivity test in Supplementary Information) and normalized to unit area to prioritize spectral *shape* over absolute intensity. Features appearing in fewer than ten molecules were excluded.

Molecules were categorized into a **12-class framework** based on:

Size: Small ($N_{\text{C}} < 50$), Medium ($50 \leq N_{\text{C}} \leq 99$), and Large ($N_{\text{C}} \geq 100$).

Charge: Anion (-1), Neutral (0), Cation ($+1$), and Dication ($+2$).

A higher-resolution 32-class grid was also utilized to validate model robustness at finer scales (see Supplementary Information).

A Random Forest (RF) classifier was trained using 500 trees and a maximum depth of 25. To address class imbalance, we applied the SMOTE (Chawla *et al.* 2002) alongside adjusted class weighting.

To simulate astronomical observations, we constructed synthetic mixtures by averaging spectra of molecules randomly drawn from an “**unseen**” pool (20% of the original data). We generated 700 mixtures per class across varying population sizes $N_{\text{mol}} \in \{1, \dots, 200\}$. Model reliability was quantified using precision, recall, and F1-scores against these controlled ground-truth mixtures.

To isolate diagnostic vibrational modes, we utilized Gini importance (Breiman 2001) across two pathways: a 4-class model for size-independent charge indicators, and four charge-specific 3-class models to isolate size-dependent features. These importance scores were mapped to IR wavelengths to pinpoint specific diagnostic signatures.

Source code, datasets, and the trained model are available on Git repository zwAstroChem (available after peer review).

RESULTS AND DISCUSSION

The RF model exhibits strong performance on the mixed PAH spectra, achieving a macro-averaged F1-score of about 0.96 (Table I). This high-fidelity classification across 12 categories demonstrates that full-profile spectral features carry sufficient information to simultaneously constrain molecular size and charge state, even for complex molecular mixtures.

TABLE I. Performance metrics (precision, recall, and F1-score) of PAH mixture classification across different size and charge categories based on the 6 eV dataset, with training sample sizes.

Category	Training	Precision	Recall	F1-score
Size				
< 50C	13 626	0.985	0.983	0.985
50–99C	4638	0.910	0.938	0.923
$\geq 100\text{C}$	663	0.975	0.992	0.983
Charge				
-1	1639	0.970	0.983	0.977
0	12 730	0.893	0.973	0.930
$+1$	2379	0.977	0.980	0.977
$+2$	2179	0.987	0.947	0.963
Average	18927	0.957	0.971	0.963

Performance varies notably with molecular size. Small PAHs ($N_{\text{C}} < 50$) achieve the highest F1-score (0.985), supported by a large training set of 13 626 spectra. Large PAHs ($N_{\text{C}} \geq 100$) perform nearly as well (F1 = 0.983) despite having only 663 training samples, which is the smallest among all size classes. This suggests that spectral features of large PAHs are sufficiently distinctive that the model requires relatively few examples to generalize accurately. In contrast, medium-sized PAHs (50–99 C) show a clear performance drop (F1 = 0.923) even though

they are reasonably well represented with 4638 training samples. An examination of the confusion matrix (Supplementary Information) reveals that systematic misclassifications primarily arise from the model's difficulty in distinguishing between size families of the same charge state, a trend driven by the broadening of spectral features as molecular size increases.

The interpretable nature of the RF model allows us to examine its “reasoning” through feature importance analysis, revealing which spectral regions are most diagnostic of PAH size and charge state. Figure 2 presents this analysis for charge state discrimination, highlighting that the model utilizes the full spectral shape rather than relying on pre-selected band ratios.

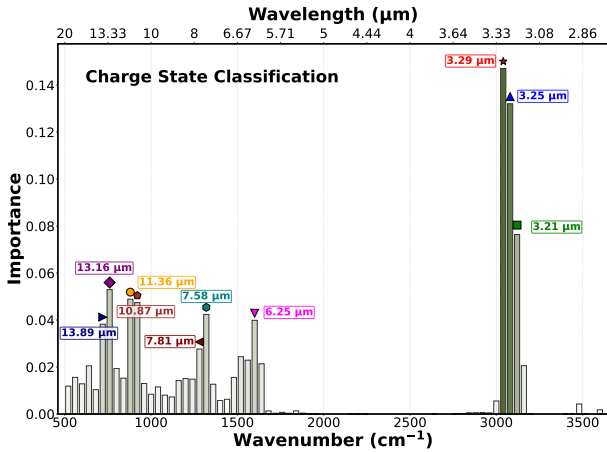


FIG. 2. Feature importance of spectral features for charge-state classification. The top 10 most influential spectral features are highlighted and labeled with their specific wavelengths.

The top 10 features identified in Figure 2 provide a nuanced perspective that corroborates and refines traditional charge diagnostics. The primary drivers for charge discrimination are the C–H stretching complex bins (centering in 3.21–3.29 μm), which receive the highest importance scores due to the characteristic suppression of the 3.3 μm band in cations (Allamandola *et al.* 1999, Bauschlicher Jr. *et al.* 2008). High importance is also assigned to C–H out-of-plane (OOP) bending modes at 11.36 and 13.16 μm (solo and trio modes), alongside features at 10.87 and 13.89 μm, which are central to ionization and size studies (Hony *et al.* 2001, Bauschlicher *et al.* 2018). Furthermore, the inclusion of C–C stretching and C–H in-plane bending features (7.58, 6.25, and 7.81 μm) underscores the model's reliance on relative intensities across the full mid-IR spectrum to constrain PAH properties.

Feature importance analysis for size classification (Figure 3) reveals that size information is distributed across multiple spectral regions in a charge-dependent manner. For neutral PAHs (Panel a), the model relies on the 3.25

and 3.29 μm bins (Draine and Li 2001, Schutte *et al.* 1993), providing a data-driven confirmation of the physical link between the 3.3 μm C–H stretch and molecular size, consistent with the classical $I_{11.2}/I_{3.3}$ proxy (Maragkoudakis *et al.* 2020).

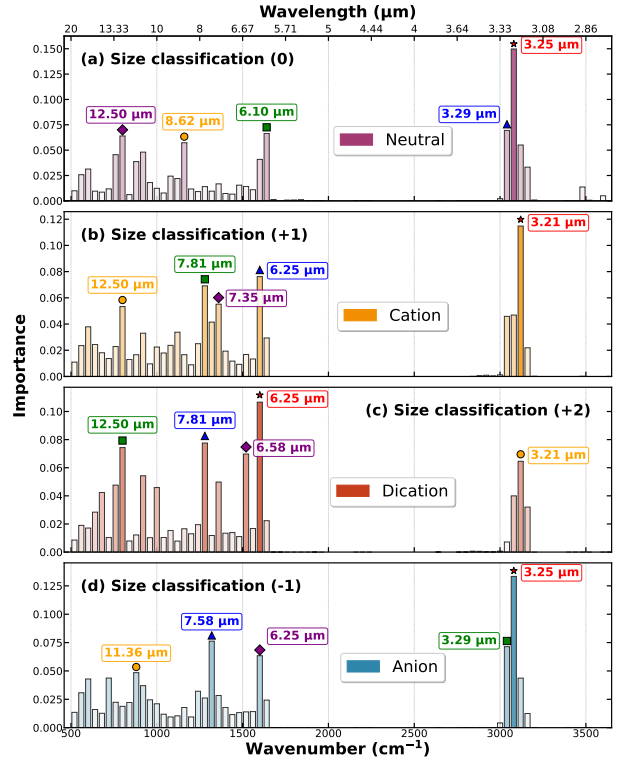


FIG. 3. Feature importance for size classification across different charge states: (a) neutral (0), (b) cation (+1), (c) dication (+2), and (d) anion (−1). Highlighted markers indicate the top 5 influential features.

For cations (Panel b) and especially dications (Panel c), diagnostic importance shifts toward the 6–8 μm C–C stretching modes at 6.25 and 7.81 μm (Peeters *et al.* 2002, Bauschlicher Jr. *et al.* 2008). The model extracts size information within these complexes, likely tracing charge-specific modifications or edge geometries, but still supports caution against using the 6.2/7.7 ratio alone for size determination. The analysis further reveals a significant departure from canonical diagnostics for anionic PAHs (Panel d), where size is primarily traced by the relative strengths of the 3.3 μm complex and the 7.58 μm C–C stretch (Allamandola *et al.* 1989, Schutte *et al.* 1993).

Figure 3 also suggests a high importance of the 12.5 μm bin across multiple charge states, particularly for ionized species (Shannon *et al.* 2015, 2016), identifies it as a robust complementary size tracer. This aligns with longer-wavelength signatures proposed as alternatives for observations lacking 3.3 μm coverage (Draine and Li 2007, Berné *et al.* 2022, Maragkoudakis *et al.* 2023, Boersma *et al.* 2024).

Furthermore, we evaluated the impact of excitation

conditions on classification performance by applying our workflow to emission spectra generated at 3, 6, and 9 eV. The classification accuracy remained remarkably consistent across these energies, maintaining F1 scores of 0.95, 0.96, and 0.95, respectively (see Supplementary Information), thereby demonstrating the robustness of our model across diverse astrophysical regimes. We also trained an auxiliary random forest model to predict excitation energy directly from the mixed spectra. The results confirm that spectral morphology serves as a reliable indicator of the local radiation environment. Detailed performance metrics for these experiments, along with results from the high-resolution 32-class validation grid, are provided in the Supplementary Information.

CONCLUSIONS

We present a ML framework to infer interstellar PAH size and charge directly from full-spectrum IR morphology. This approach circumvents the information loss and sample-selection bias inherent to traditional band-ratio diagnostics. When evaluated on synthetic realistic mixtures from an unseen molecular pool, the model achieves robust performance across 12 size and charge classes, yielding a macro F1-score near 0.96. Feature importance analysis reveals distinct spectral fingerprints: neutral PAHs are primarily classified via the 3.21–3.29 μm and 11–14 μm regions, while charge discrimination in ions relies increasingly on C–C stretching modes at 6.25 and 7.81 μm . The 12.5 μm feature emerges as a robust, complementary tracer of molecular size across all charge states. Additionally, we show that excitation conditions leave distinct, detectable imprints on spectral morphology.

*zw@gxu.edu.cn

A. Leger and J. L. Puget, *A&A* **137**, L5 (1984).
 L. J. Allamandola, A. G. G. M. Tielens, and J. R. Barker, *ApJ* **290**, L25 (1985).
 E. Peeters, S. Hony, C. Van Kerckhoven, A. G. G. M. Tielens, L. J. Allamandola, D. M. Hudgins, and C. W. Bauschlicher,

- A&A* **390**, 1089 (2002).
 J. D. T. Smith *et al.*, *ApJ* **656**, 770 (2007).
 E. L. O. Bakes and A. G. G. M. Tielens, *ApJ* **427**, 822 (1994).
 L. J. Allamandola, D. M. Hudgins, and S. A. Sandford, *ApJ* **511**, L115 (1999).
 A. G. G. M. Tielens, *ARA&A* **46**, 289 (2008).
 A. Li, *Nat. Astron.* **4**, 339 (2020).
 B. T. Draine and A. Li, *ApJ* **551**, 807 (2001).
 L. J. Allamandola, A. G. G. M. Tielens, and J. R. Barker, *ApJS* **71**, 733 (1989).
 W. A. Schutte, A. G. G. M. Tielens, and L. J. Allamandola, *ApJ* **415**, 397 (1993).
 C. Boersma, J. Bregman, and L. J. Allamandola, *ApJ* **858**, 67 (2018).
 A. Maragkoudakis, E. Peeters, and A. Ricca, *MNRAS* **494**, 642 (2020).
 C. W. Bauschlicher Jr., E. Peeters, and L. J. Allamandola, *ApJ* **678**, 316 (2008).
 A. Ricca, C. W. Bauschlicher Jr., C. Boersma, A. G. G. M. Tielens, and L. J. Allamandola, *ApJ* **754**, 75 (2012).
 C. W. Bauschlicher Jr. and A. Ricca, *Mol Phys* **108**, 2647 (2010).
 C. Boersma, C. W. Bauschlicher Jr., A. Ricca, A. L. Mattioda, J. Cami, E. Peeters, F. S. de Armas, G. P. Saborido, D. M. Hudgins, and L. J. Allamandola, *ApJS* **211**, 8 (2014).
 E. Peeters, C. W. J. Bauschlicher, L. J. Allamandola, A. G. G. M. Tielens, A. Ricca, and M. G. Wolfire, *ApJ* **836**, 198 (2017).
 A. Ricca, C. Boersma, A. Maragkoudakis, J. E. Roser, M. J. Shannon, L. J. Allamandola, and C. W. Bauschlicher, Jr., *ApJS* **282**, 7 (2026).
 C. W. Bauschlicher and S. R. Langhoff, *AcSpA* **53**, 1225 (1997).
 N. V. Chawla, K. W. Bowyer, L. O. Hall, and W. P. Kegelmeyer, *J. Art. Intel. Res.* **16**, 321 (2002).
 L. Breiman, *Machine Learning* **45**, 5 (2001).
 S. Hony, C. Van Kerckhoven, E. Peeters, *et al.*, *A&A* **370**, 1030 (2001).
 C. W. Bauschlicher *et al.*, *ApJ* **866**, 21 (2018).
 M. J. Shannon, D. J. Stock, and E. Peeters, *ApJ* **811**, 153 (2015).
 M. J. Shannon, D. J. Stock, and E. Peeters, *ApJ* **824**, 111 (2016).
 B. T. Draine and A. Li, *ApJ* **657**, 810 (2007).
 O. Berné *et al.*, *A&A* (2022).
 A. Maragkoudakis, E. Peeters, and A. Ricca, *MNRAS* **524**, 3429 (2023).
 C. Boersma *et al.*, *ApJ* **975**, 177 (2024).